JOURNAL OF GEOPHYSICAL RESEARCH, VOL. 112, B04305, doi:10.1029/2006JB004395, 2007

Spatial and temporal stress drop variations in small earthquakes near Parkfield, California

Bettina P. Allmann[1] and Peter M. Shearer[1]

Received 14 March 2006; revised 24 October 2006; accepted 27 November 2006; published 12 April 2007.

[1] We estimate source parameters from spectra of 42367 earthquakes between 1984 and 2005 that occurred in the Parkfield segment of the San Andreas Fault in central California. We use a method that isolates the source term of the displacement spectra based on a convolutional model and correct the observed P wave source spectra with a spatially varying empirical Green's function (EGF). Our Brune-type stress drop estimates vary from 0.1 to over 100 MPa with a median value of 6.75 MPa, which is nearly constant with moment, implying self-similarity over the M_L = 0.5 to 3.0 range of our data. The corner frequency decreases for earthquakes at shallower depths, consistent with slower rupture velocities and reduced shear wave velocities in local velocity models. The estimated median stress drops show significant lateral variations: we find lower stress drops in the Middle Mountain asperity and along the creeping fault section, and higher stress drops in the hypocentral region of the 2004 M6.0 Parkfield earthquake. The main shock did not alter the overall pattern of high and low stress drop regions. However, a statistical test reveals areas with significant changes in computed stress drops after the main shock, which we compare to estimated absolute shear stress changes from a main shock slip model. By calculating Δt^* from the spectral EGF ratio, we also identify areas with increased attenuation after the main shock, and we are able to distinguish source effects and near-source attenuation effects in the spectral analysis. These results are confirmed independently from spectral ratios of repeating microearthquake clusters.

Citation: Allmann, B. P., and P. M. Shearer (2007), Spatial and temporal stress drop variations in small earthquakes near Parkfield, California, *J. Geophys. Res.*, *112*, B04305, doi:10.1029/2006JB004395.

1. Introduction

[2] Investigation of source parameters for most earthquakes uses far-field recordings of the radiated seismic energy. One of the most important source parameters that can be estimated seismically is the stress drop $\Delta\sigma$, i.e., the difference between the average state of stress on the fault plane before and after an earthquake. Using the source model of *Brune* [1970] and *Madariaga* [1976], the stress drop is estimated from the shape of the source spectrum, which is described by the corner frequency [e.g., *Boatwright*, 1984].

[3] The accurate determination of stress drops is difficult in practice for two reasons:

[4] 1. The number of reliably measurable observables in the spectrum is typically smaller than the number of free parameters in a particular source model. Therefore stress drop determination depends on a priori assumptions made in the source model [e.g., *Brune et al.*, 1979]. This fact makes it difficult to compare different studies of stress drop.

[5] 2. The medium through which the seismic energy propagates may cause a similar imprint on the far-field seismic signature as the source itself. It is therefore difficult to separate contributions of source and propagation path effects in far-field seismic spectra, which is especially relevant for smaller size earthquakes ($M < 4.0$). The latter problem is traditionally addressed with an empirical Green's function (EGF) correction [*Mueller*, 1985; *Hough*, 1997], in which the source spectrum is deconvolved with one or more nearby smaller earthquakes for which we can assume the spectrum to be nearly flat over the frequency range of interest. The deconvolution thus corrects for the path effects between the source and the receiver. The higher frequencies contained in small earthquakes make it more difficult to correct the source spectra for attenuation, especially if the data are recorded at the surface [*Anderson*, 1986]. Consequently, the most reliable source parameter determinations obtained so far for $M < 2$ earthquakes stem from data recorded in boreholes [e.g., *Abercrombie*, 1995; *Ide et al.*, 2003; *Imanishi et al.*, 2004].

[6] If many earthquakes are recorded at many receivers, *Warren and Shearer* [2002] have recently introduced a method to separate source spectra based on a convolutional model. This approach has been successfully applied to earthquake data from Anza, California, [*Prieto et al.*, 2004] and the whole of southern California [*Shearer et al.*, 2006]. The method exploits the redundancy obtained

[1]Cecil H. and Ida M. Green Institute of Geophysics and Planetary Physics, Scripps Institution of Oceanography, University of California, San Diego, La Jolla, California, USA.

0148-0227/07/2006JB004395$09.00

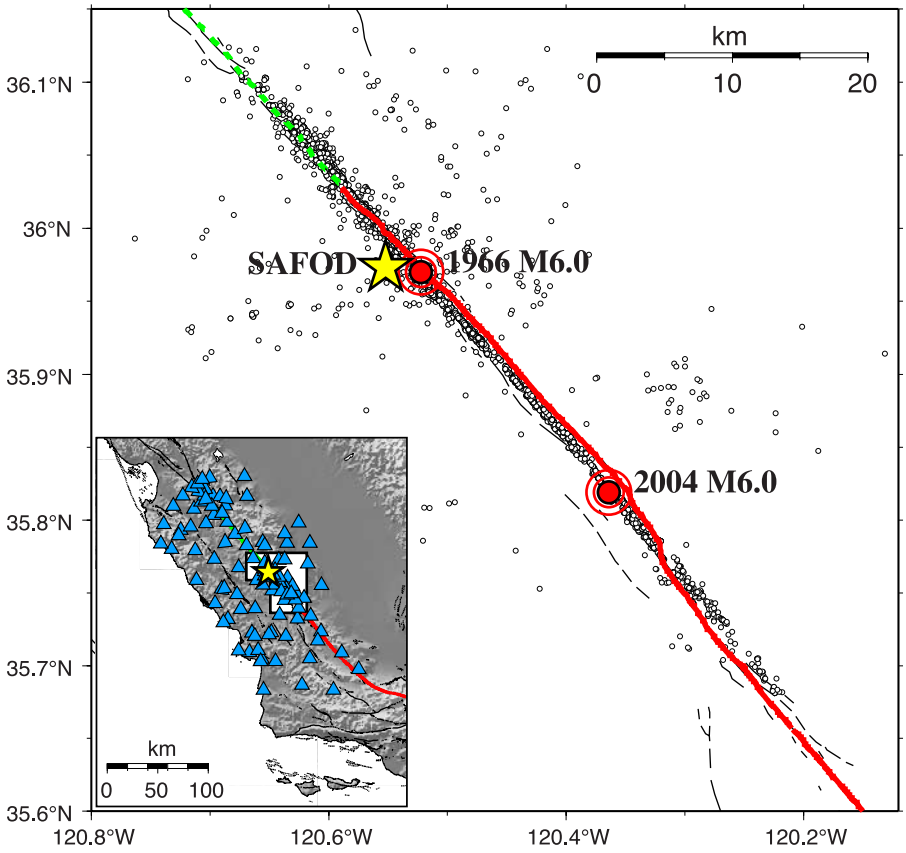

Figure 1. Stations (triangles) and earthquakes (circles) along the Parkfield segment of the San Andreas fault (SAF). The 4346 events, recorded at 204 stations, were used in the analysis. The creeping section of the SAF is shown as a dashed line, and the locked section is shown as a solid line. The epicenters of the 1966 M6.0 and 2004 M6.0 main shocks are shown as big circles. The location of the San Andreas Fault Observatory at Depth (SAFOD) is marked as a star.

from a large number of overlapping source-receiver pairs to solve for empirical source, station, and propagation path terms. It provides a method to estimate source parameters for an entire region in a consistent way. It is therefore particularly suited to investigate relative changes in source parameters of small earthquakes.

[7] In this paper, we apply this method to seismicity along the San Andreas Fault (SAF) surrounding the San Andreas Fault Observatory at Depth (SAFOD) near Parkfield, California. The Parkfield segment of the SAF is the most intensively studied fault in the world [e.g., *Roeloffs and Langbein*, 1994; *Fletcher and Spudich*, 1998; *Fletcher and Guatteri*, 1999; *Nadeau and Johnson*, 1998; *Abercrombie*, 2000; *Thurber et al.*, 2003, 2004; *Murray and Segall*, 2005]. It forms the transition from the aseismically creeping section (northwest) to a locked section (southeast) on which major earthquakes can occur [*Wallace*, 1990]. Parkfield is also the nucleation area of repeating $M \approx 6$ earthquakes. The most recent of these characteristic events occurred on 28 September 2004 [e.g., *Langbein et al.*, 2005]. Thousands of well-recorded microearthquakes have also occurred in this segment during the last 20 years [e.g., *Nadeau and Johnson* 1998]. Furthermore, asperities and other lateral variations of fault zone properties have been mapped [e.g., *Schorlemmer et al.*, 2004; *Korneev et al.*, 2003; *Chavarria et al.*, 2004], making the Parkfield region a prime candidate to test for lateral variations of stress drop.

2. Data and Method

[8] Our processing approach generally follows that of *Shearer et al.* [2006], to which the reader is referred for additional details. We selected waveform data from the Northern California Earthquake Data Center (NCEDC) of about 10,000 events that occurred between 1984 and 2005 in a 70 km wide segment of the San Andreas Fault (SAF) in the vicinity of the 2004 M6.0 Parkfield earthquake (Figure 1). We compute displacement spectra of short-period vertical component instruments using the multitaper method of *Park et al.* [1987] for 1.28 s windows before (noise) and after (signal) the picked P arrival. The data are sampled at 100 Hz. We require a signal-to-noise ratio of three or greater between the frequency bands 1 to 5 Hz, 5 to 10 Hz, and 10 to 20 Hz, respectively, for all spectra. We also require each event to be recorded at this signal-to-noise level by at least five different stations. This restriction is intended both to better isolate station terms, and to average out directivity effects, which can affect the source parameter estimation [e.g., *Venkataraman and Kanamori*, 2004b]. We assume that the displacement spectra $d_{ij}(f)$ of source i and receiver j can be described in the log domain by a linear

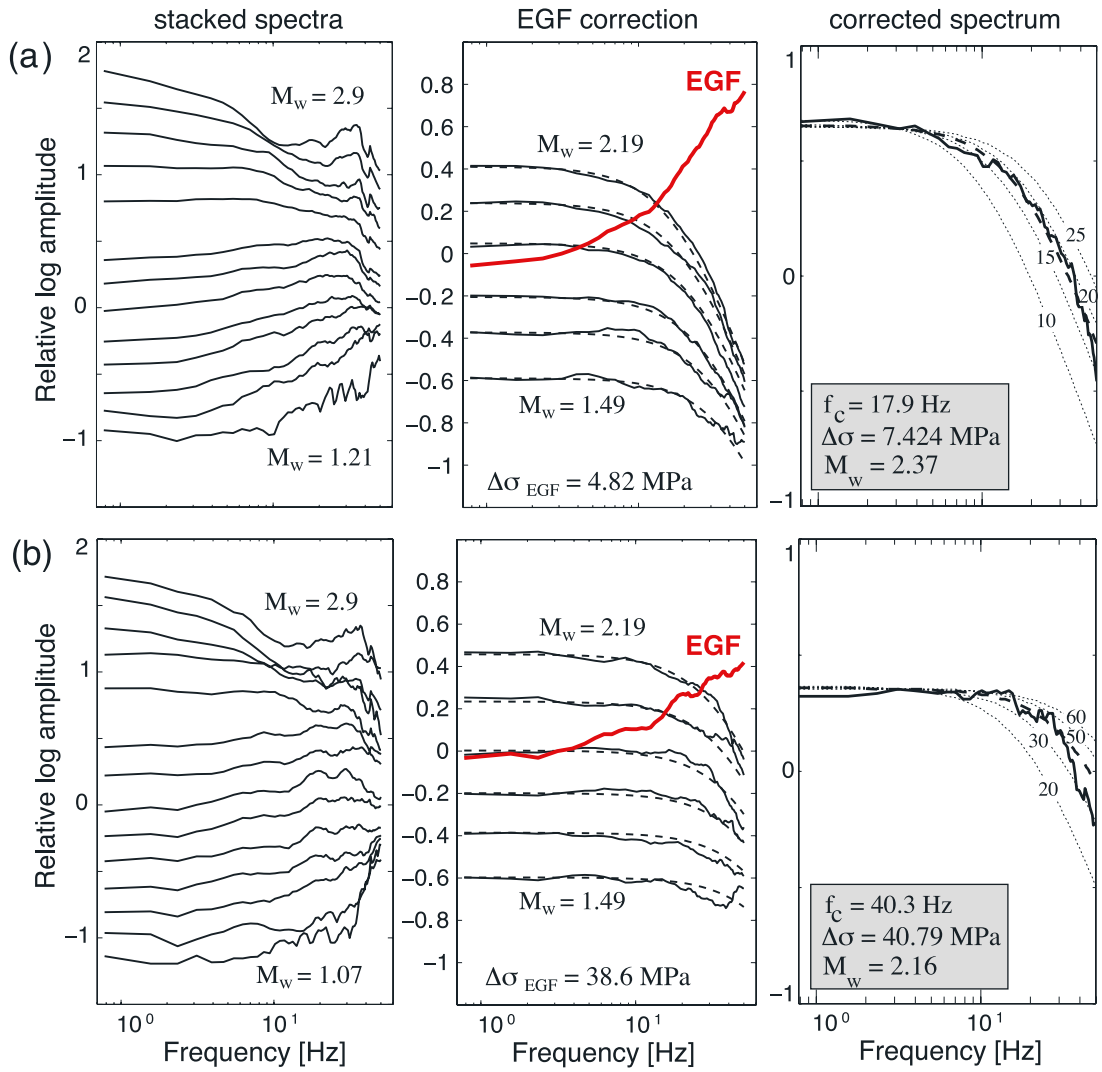

Figure 2. Two example events: (a) one for a medium stress drop region and (b) one for a high stress drop region, see $\Delta\sigma_{\mathrm{EGF}}$. The NCSN cuspid numbers are 201333 and 21224977, respectively. (left) Stacked source spectra in 0.2 local magnitude increments over 200 events. The lower and upper moment magnitude bounds are marked. (middle) EGF-corrected spectra (solid) in comparison to theoretical spectra (dashed). The bold solid curve shows the EGF, which was computed over a moment magnitude range from 1.49 to 2.19. (right) EGF-corrected source spectra of the respective target event (solid) together with the best fitting theoretical spectrum (dashed) and a range of theoretical spectra for varying corner frequencies around the best fit (dotted). The corner frequencies in Hz are indicated as numbers along the curves. The best fitting corner frequencies f_c and resulting stress drops $\Delta\sigma$ are also indicated.

combination of a source term e_i, a receiver term s_j and a traveltime-dependent term $t_{k(i,j)}$:

$$d_{ij} = e_i + s_j + t_{k(i,j)} + r_{ij}, \tag{1}$$

where r_{ij} is a residual term. Using equation (1), we can isolate the source term e_i of the displacement spectra by means of an iterative robust least squares approach [*Shearer et al.*, 2006]. We can estimate the relative seismic moment Ω_0 of each event from the isolated source term e_i. Ω_0 is estimated from the amplitude of the low-frequency part of the spectra (which we take to be the mean amplitude between 2.3 and 3.8 Hz in each source spectra) and can be calibrated to absolute seismic moment M_0 using the local magnitude M_L. For the calibration, we assume equality of local and moment magnitude at $M_w = M_L = 3.0$.

[9] The resulting relative source spectra need to be deconvolved with an empirical Green's function (EGF) in order to obtain reliable estimates of the corner frequency of individual events. We achieve this by stacking all relative source spectra of the closest 200 neighboring events for each target event into bins of equal moment, and fit the binned source spectra with a theoretical source model within each moment bin. Figure 2 (left) shows the stacks for two example target events. We simultaneously fit a constant parameter source model and estimate the EGF by

averaging the differences between observed and theoretical log spectra over all bins for every frequency sample (Figure 2, middle). In other words, we determine a spatially varying EGF for each individual event from stacking the source spectra of the closest 200 neighboring events in 0.2 units of estimated local magnitude. Using a fixed number of events to calculate the EGF results in a varying volume over which the EGF is averaged. In areas of higher seismicity the volume is smaller, whereas in areas of sparse seismicity the volume is larger. We compute the EGF over a range from 0.9 to 1.9 of estimated local magnitude, which corresponds to a moment magnitude range from 1.49 to 2.19. Below and above this magnitude range, the number of events per magnitude bin is too small to obtain a stable estimate of the EGF. The stress drops of the best fitting models for the EGF estimations from the 200 events around the two target events are 4.82 MPa for the medium stress drop region (Figure 2a, middle) and 38.6 MPa for the high stress drop region (Figure 2b, middle). Figure 2 (right) shows the EGF-corrected source spectra for the two example events. Dotted lines show the theoretical spectra for a range of corner frequencies, including the best fitting result of the least squares procedure (bold dashed).

[10] We use the spectral shape proposed by *Brune* [1970]:

$$u(f) = \frac{\Omega_0}{1 + (f/f_c)^n}, \tag{2}$$

where Ω_0 is the long-period amplitude, f_c is the corner frequency, and n is the high-frequency falloff rate. We set $n = 2$ (ω^{-2} model), which is the most commonly used value and gives a good overall fit to our data.

[11] Assuming a circular fault, the stress drop $\Delta\sigma$ can be calculated from the seismic moment M_0 and the source radius r [*Eshelby*, 1957]:

$$\Delta\sigma = \frac{7}{16}\left(\frac{M_0}{r^3}\right) \quad . \tag{3}$$

The source radius can be related to the corner frequency [*Madariaga*, 1976]:

$$f_c = 0.32\frac{\beta}{r}\ , \tag{4}$$

where β is the shear wave velocity near the source, and the rupture velocity is assumed to be 0.9 β. Combining equations (3) and (4), we obtain

$$\Delta\sigma = M_0\left(\frac{f_c}{0.42\beta}\right)^3\ , \tag{5}$$

where we will refer to $\Delta\sigma$ as stress drop. The reader should bear in mind, however, that these Brune-type stress drop estimates are not necessarily equal to the true static stress drop of the earthquake (for further discussions, see, e.g., *Andrews* [1986], *Snoke* [1987], and *Hough* [1996]).

[12] After correcting the individual source spectra by subtracting the respective EGF, we can compute the stress drop from the best fitting corner frequency using equation (5). We obtain the corner frequency from a least squares fit of the deconvolved log spectrum with the theoretical spectrum between 1 and 20 Hz. A higher frequency band might allow a smaller uncertainty in determining corner frequencies beyond the fitting range, but the signal-to-noise ratio for most records deteriorates rapidly for higher frequencies. We tested several different fitting ranges and found 1–20 Hz to yield the most reliable results for the widest magnitude range. Note that we are able to resolve corner frequencies above this fitting range and that the resolution limit of our data does not necessarily depend on the Nyquist frequency (50 Hz). However, the reliability of our estimates decreases with increasing corner frequencies beyond the fitting range, as shown in Appendix A, which presents synthetic tests of the performance of our algorithm. The higher the corner frequency, the smaller is the curvature of the spectrum within the fitting range, and thus the higher are the uncertainties of the least squares fit. As a consequence, we assign the upper bound of the corner frequency iteration to be 100 Hz. Because of these limitations there is no clearly defined upper resolution limit of our corner frequency and stress drop estimates.

[13] This processing leads to stress drop estimates for 4346 events. The individual event stress drops are subject to large scatter. This is caused by a combination of effects, such as the uncertainty in corner frequency estimation, simplified assumptions of the source model, incomplete averaging of radiation pattern effects, or real heterogeneities of physical properties along the fault. In consideration of the uncertainties, the individual stress drop estimate for a particular event might generally not be representative of a region, and thus we concentrate on properties derived from the data in a statistical sense. Assuming the unwanted sources of scatter are spatially uncorrelated, we can extract the long-wavelength spatial variations of the stress drop estimates by applying a seismicity-based median filter to the data. Such spatial stress drop variations along the fault plane of the SAF reflect heterogeneities of fault properties. We therefore assign the event stress drop to the relocated hypocenter location and smooth our result by applying a spatial median filter over 50 events. All events were relocated using the shrinking box method proposed by *Shearer et al.* [2005] and *Lin and Shearer* [2005]. For a better visualization of spatial stress drop variations along the fault plane, we project all relocated events within a distance of ±1 km of the fault onto the fault plane and apply a nearest neighbor gridding algorithm with a grid spacing of 1 km by 1 km [*Smith and Wessel*, 1990].

[14] This method to compute earthquake source parameters based on many events allows a robust determination of relative stress drop changes in space and time over our study area, which will be the focus of the analysis that follows.

3. Stress Drop Results

[15] The individual event stress drops are very heterogeneous and span 4 orders of magnitude, ranging from 0.1 to over 1000 MPa, although the upper limit is not reliably determined because of the decrease of resolution for corner frequencies beyond the fitting range. We obtain a median stress drop of 6.75 MPa over all 4238 events within ±1 km of the fault zone. The bulk of the stress drop values are between 1 and 40 MPa, which is comparable to results

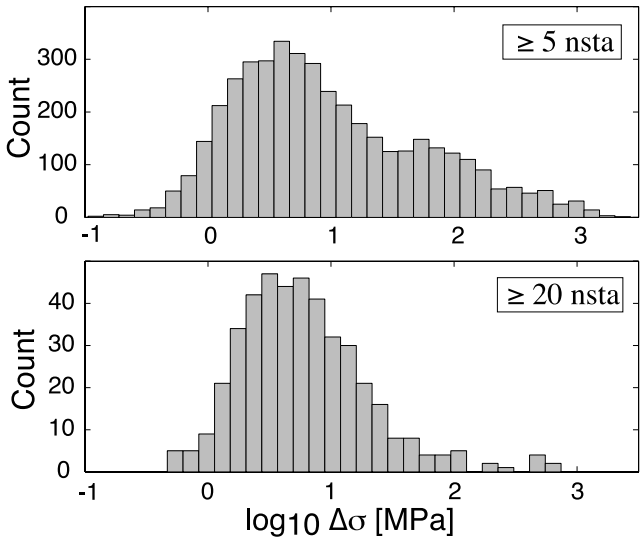

Figure 3. Histogram of stress drop estimates requiring at least (top) 5 and (bottom) 20 station recordings per event.

observed in other studies [e.g., *Abercrombie*, 1995; *Prejean and Ellsworth*, 2001; *Shearer et al.*, 2006]. The histogram in Figure 3 shows the distribution of log stress drops for a different minimum number of station recordings per event. The scatter in the stress drop distribution can be significantly reduced by increasing the required number of stations. Also, the higher the minimum number of stations, the more the distribution resembles a Gaussian. This is because stress drops are increasingly difficult to resolve for smaller magnitude events. Events that were recorded by more stations are usually larger and allow a more reliable determination of stress drop. The asymmetric distribution and higher scatter for a minimum of five stations (Figure 3a) is therefore caused by larger uncertainties in the stress drop estimates of small events due to very high corner frequencies and the large degree of variability in the individual spectra.

[16] In the following, we will require a minimum number of five stations per event, despite the bias in the distribution. This still allows us to resolve the variations in median stress drop and it is preferable to requiring more stations, because (1) we have a larger magnitude bandwidth to work with and (2) we have a larger overall number of events. While the former is necessary for a reliable determination of the EGF, the latter is needed to obtain a uniform spatial distribution for interpolating stress drops over the fault surface.

3.1. Moment Dependence

[17] One controversial question about stress drop is its dependence or independence of moment. Self-similarity of earthquakes, i.e., scale invariance of earthquake source mechanics, was first suggested by *Aki* [1967]. Lower stress drops for smaller magnitudes have been observed by several authors [e.g., *Archuleta et al.*, 1982]. Such an observation could mean that earthquakes are not self-similar. Other authors explain this apparent breakdown of self-similarity for smaller magnitude events to be caused by either bias related to attenuation of higher frequencies [e.g., *Anderson*, 1986; *Abercrombie*, 1995; *Ide et al.*, 2003] or due to a limited bandwidth of the data [e.g., *Hough*, 1996; *Ide and Beroza*, 2001].

[18] Similar to the results of *Kanamori and Anderson* [1975], and *Abercrombie* [1995] we do not observe any

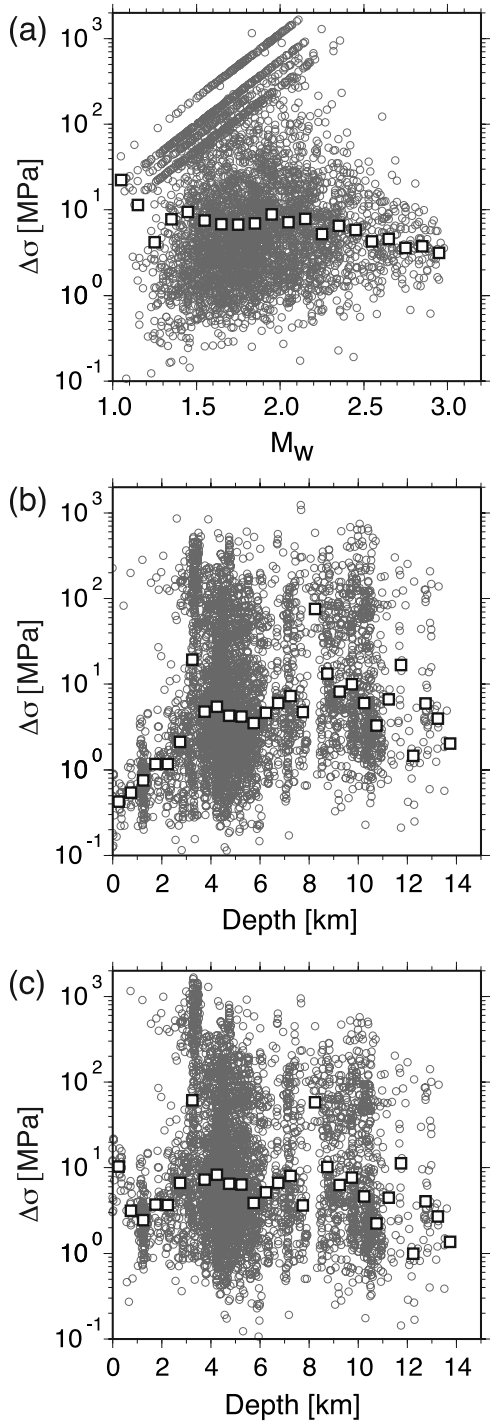

Figure 4. (a) Stress drop versus moment magnitude. The squares mark the median stress drop. There is no obvious correlation between stress drop and moment magnitude. (b) Stress drop estimates computed assuming a constant shear wave velocity. (c) Stress drop estimates computed assuming a depth-varying shear wave velocity. Note that the computed stress drops increase with depth for Figure 4b but not for Figure 4c.

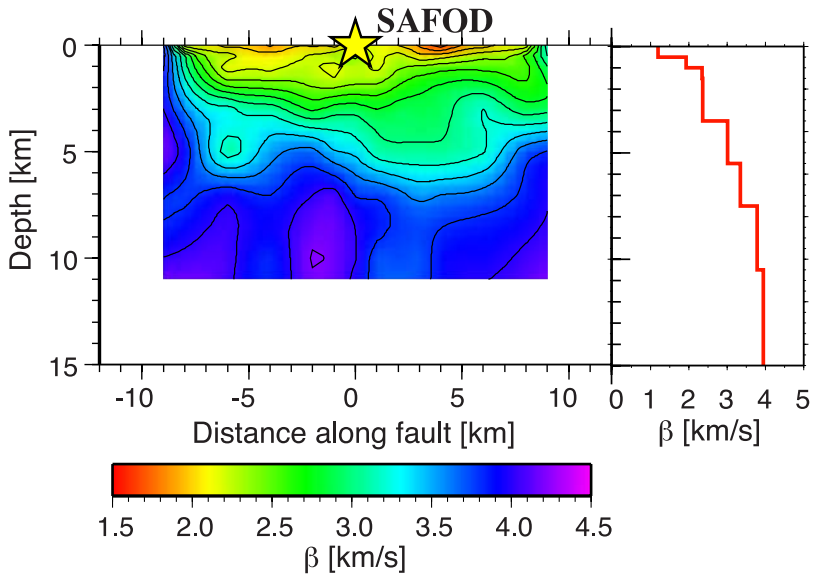

Figure 5. (left) SAF slice from the 3-D shear wave velocity model of *Thurber et al.* [2004]. (right) Horizontal mean of shear wave velocity.

correlation between median stress drop and moment magnitude in our data (Figure 4a). Apart from the independence of stress drop from magnitude, Figure 4a also shows the resolution limit of our data. The upper boundary of determined stress drop values is a set of parallel lines corresponding to the maximum corner frequency (100 Hz) assigned in our analysis method. Corner frequencies this high (and their corresponding stress drops) are not reliably resolved, but still need to be considered for an accurate calculation of median stress drop within bins of constant moment magnitude. Stress drops in Figure 4a have been calculated from corner frequencies using a depth-dependent shear wave velocity, which causes the resolution limit to show as a set of parallel lines, instead of one line.

3.2. Depth Dependence

[19] Various authors have reported an increase of stress drop with depth [e.g., *Jones and Helmberger*, 1996; *Hardebeck and Hauksson*, 1997; *Venkataraman and Kanamori*, 2004a]. In southern California, *Shearer et al.* [2006] observe a median stress drop increase from 0.6 MPa near the surface to 2.2 MPa at 8 km depth, assuming a constant rupture velocity. For their stress drop estimates, they used equation (5) with a constant shear wave velocity of 3.464 km/s. Using the same calculation, and calculating median stress drops over 0.5 km depth bins, we also observe an apparent increase of stress drop with depth in the upper 10 km (Figure 4b). Since the stress drop varies as a power of three with shear wave velocity β, the assumption of a constant β likely biases the increase of stress drop in the upper crust. On the other hand, β from equation (5) also scales with the rupture velocity, and therefore a varying shear wave velocity implies that we assume the rupture velocity to vary with depth. The Parkfield area offers the advantage that high-resolution tomographic velocity models are available [e.g., *Michelini and McEvilly*, 1991; *Eberhart-Phillips and Michael*, 1993; *Thurber et al.*, 2004]. In this case, we can correct our stress drop data with a velocity-depth function obtained from averaging the three-dimensional (3-D) velocity model by *Thurber et al.* [2004] horizontally along the trace of the SAF (see Figure 5). In this velocity model, the fault zone itself shows lower shear wave velocities than the surrounding crust in the upper 5 km. Although the model only extends over a part of the investigation area (±10 km around SAFOD), the available velocity information is sufficient to capture the average depth dependence of β in the area.

[20] As a consequence, we observe that much of the apparent depth dependence of median stress drop can be removed by estimating stress drops using a depth-varying shear wave velocity (Figure 4c), which is equivalent to the assumption of slower rupture velocities at shallow depth. We cannot definitively resolve an increase of stress drop with depth from our data in the Parkfield region but we have shown that any depth dependence of stress drop is very sensitive to the chosen velocity model. A statistical test of the depth dependence (as carried out, e.g., by [*Hardebeck and Hauksson*, 1997]) may lead to biased results due to errors or lateral variations in the velocity model. An apparent decrease of median stress drops at depths greater than 10 km in our data is most likely caused by a spatial bias: most events below 10 km are located in the Middle Mountain asperity, a region where we generally observe lower stress drops.

[21] We should point out that the correction with a variable shear wave velocity does not alter the general observation of a decrease in high-frequency radiation at shallow depths. We simply offer an alternative explanation: a slower shear wave velocity at shallow depths means a slower rupture velocity if we assume a constant scaling between rupture velocity and shear wave velocity. Ultimately, our data do not distinguish between depth-dependent rupture velocities and depth-dependent stress drops.

3.3. Lateral Variations

[22] Figure 6a shows a cross section along the fault plane with all events within ±1 km projected onto the fault. We observe significant lateral stress drop variations. An area of

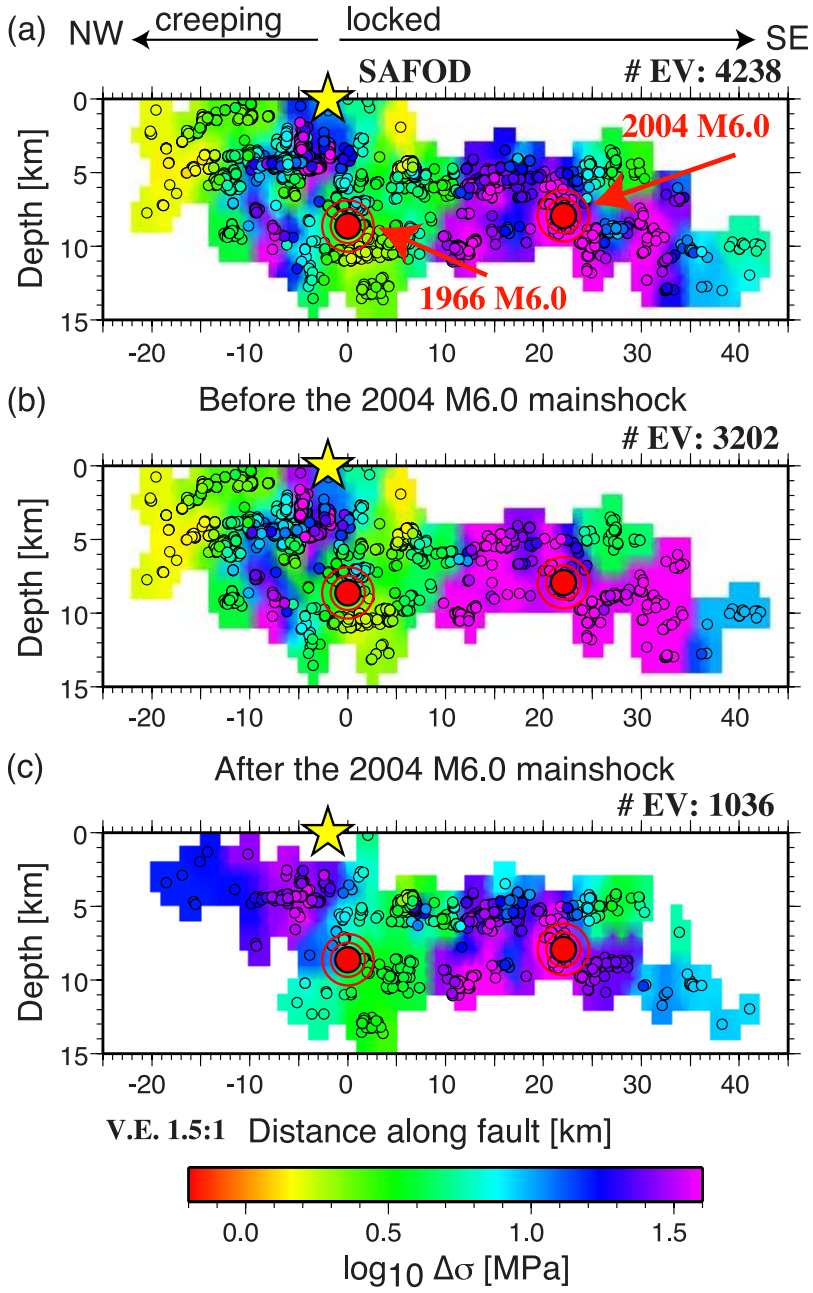

Figure 6. Spatial and temporal stress drop variations along the SAF. Small circles show all events projected onto the fault plane. The 1966 and 2004 hypocenters are shown as big circles. (a) Spatial stress drop variations over the whole time period from 1984 to June 2005. (b) Stress drop variations before the 2004 M6.0 main shock. (c) Stress drop variations after the 2004 M6.0 main shock.

very high stress drop events is observed around the 2004 M6.0 main shock, with values between 15 and 40 MPa. The so-called Middle Mountain asperity below the 1966 M6.0 hypocenter shows significantly lower stress drop values (less than 5 MPa) compared to the surrounding areas. The creeping section, starting northwest of SAFOD, shows equally low stress drop events with values below 5 MPa. These spatial variations do not change significantly for different choices of the free parameters of the source model, such as, e.g., the falloff rate. Likewise, other processing parameters such as the number of neighboring events for the EGF calculation or the width of the median filter have only little effect on the long wavelength component of spatial variations. Our choice of 200 events to calculate the EGF represents a compromise reflecting the trade-off between the number of events required in each moment bin for a reliable least squares fit and the size of the volume in which the EGF is averaged. The fault area spanned by the EGF events varies from about 1 km^2 in regions of dense seismicity to about 400 km^2 on the perimeter of our study area. We also do not observe an obvious correlation between spatial stress drop variations and existing tomographic velocity models of the area (Figure 5). However, regions of high P wave to S wave velocity ratio at shallow depths in the vicinity of the

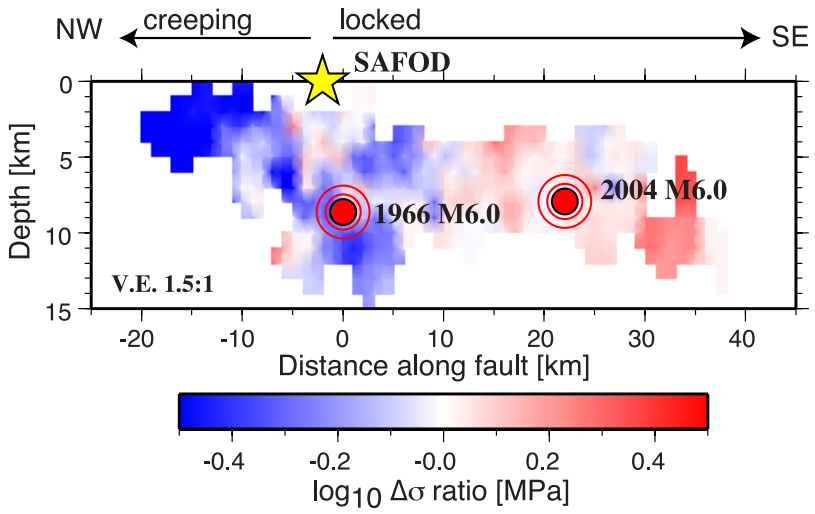

Figure 7. Ratio of stress drop before and after the 2004 M6.0 Parkfield earthquake, computed assuming no change in attenuation. Negative values denote a possible increase of stress drop after the event and positive values denote a decrease.

1966 hypocenter have been observed [*Michelini and McEvilly*, 1991; *Thurber et al.*, 2003].

3.4. Temporal Variations

[23] For an understanding of the physics of earthquakes it is important to know if a long-term change in the fault zone induced by a large event can have an effect on source parameters of smaller events within the affected zone (aftershocks). Or, if the latter is true, whether differing source parameters of aftershocks allow us to infer changes in the physical properties of the fault zone, i.e., the shear stress on the fault. We therefore examine the possibility of temporal stress drop variations due to the 2004 M6.0 Parkfield earthquake by splitting the whole data set into events before and after the main shock. The M6.0 2004 main shock was the largest earthquake over the investigation period (1984–2005) and thus the most likely candidate for long-term changes within the fault zone. Figures 6b and 6c show the stress drop results before and after the 2004 main shock. Despite the different locations and number of events before and after the main shock, the overall pattern of lateral stress drop variations along most of the fault does not change. We still observe the highest stress drop events around the main shock and lower stress drop results in the Middle Mountain region. The increased stress drop values observed along the creeping section northwest of SAFOD are not very well constrained because the width of the median filter (50 events) is much larger than the number of events observed in this region after the M6.0 2004 earthquake (<10 events).

[24] The difference between stress drops before and after the 2004 earthquake is shown in Figure 7. Here the logarithm of the ratio between every nonzero grid point before and after is depicted. We take the ratio instead of the difference in order to emphasize relative changes in stress drop. Since stress drops are varying over several orders of magnitude, the absolute value of stress drop change would not be very meaningful. Negative values in Figure 7 refer to an increase in stress drop after the 2004 event, whereas positive values denote an overall decrease of aftershock stress drops. In this case, events up to 9 months after the earthquake (June 2005) are considered in the analysis. We observe that the Middle Mountain asperity below the 1966 M6.0 hypocenter shows an increase by almost a factor of 2. The creeping section shows an even stronger increase by a factor of 3 or more. Changes in the vicinity of the 2004 hypocenter are much less pronounced but appear as a slight decrease in Figure 7.

[25] To test for the statistic significance of temporal stress drop changes we apply the bootstrap method, which is a measure of variability and bias. We randomly generate 100 resamples of the original data distribution. This is done separately for all events before and after the 2004 main shock. For all of our resamples we interpolate stress drops onto a surface using a nearest neighbor gridding algorithm. For every grid point we now compute the mean, μ, and the standard deviation, σ, over all resamples of the logarithmic ratio between before and after, with σ thus representing the bootstrap estimate of the standard error in μ. For the purpose of identifying areas with statistically significant temporal changes, we calculate the log ratio between the mean and standard deviation:

$$s = \log_{10} \frac{|\mu|}{\sigma}. \tag{6}$$

This ratio is shown in Figure 8. If the estimated standard error is equal to the mean, the logarithm of the ratio is zero. If the mean of the ratio between stress drops before and after over all resamples is bigger than its estimated standard error ($s \geq 0$), we can state that the temporal change is statistically significant at the 68% level. If $s \geq 0.3$, then $|\mu|$ is over twice as large as its estimated standard error and thus significant at the 95% level. For the opposite case, when the standard error is bigger than the mean, the temporal changes do not differ significantly from zero and are either not resolvable or nonexistent. Figure 8 shows that we observe statistically significant changes due to the 2004 M6.0 earthquake in some, but not all, areas of the Parkfield fault segment.

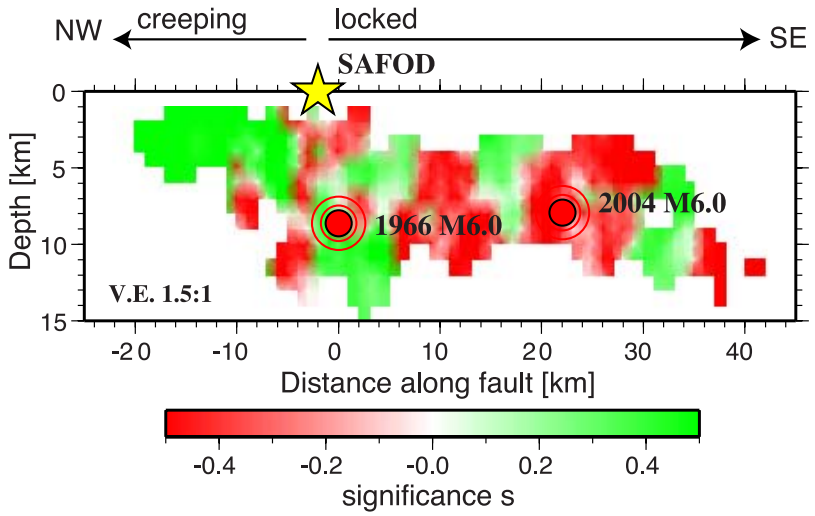

Figure 8. Logarithmic ratio between mean and estimated standard error computed over 100 resamples of the difference between before and after the 2004 main shock after applying the bootstrap method. Positive numbers indicate areas with statistically significant temporal stress drop changes with $s \geq 0.3$ being significant at the 95% level. Negative numbers are areas with no or not resolvable temporal changes.

Especially in the Middle Mountain asperity, below the 1966 M6.0 hypocenter, we observe a temporal change of stress drop aftershocks that is highly significant compared to the estimated standard error. We also observe significant changes in the vicinity of the 2004 main shock. The positive significance observed along the creeping section northwest of SAFOD is again an effect of using a median filter that is larger than the number of events after the main shock in this particular region.

3.5. Correcting for Attenuation Changes

[26] So far in our analysis, the resulting temporal stress drop variations are derived from a calculation, in which we did not account for the possibility of changes in the medium due to the M6.0 main shock. To test for this, we performed a separate spectral analysis and EGF correction before and after the main shock. In this case, we might expect medium changes in the core of the fault zone, i.e., close to the source. Such medium changes are difficult to resolve by the spectral separation method alone, and require also a separate EGF correction. Temporal stress drop variations derived from separately reprocessing the data yield a similar result for the regions of stress drop increase shown in Figure 9: We still obtain a significant increase in stress drop in the Middle Mountain asperity and the creeping section. However, in the vicinity of the 2004 M6.0 hypocenter, we obtain a stress drop increase instead of a decrease. This could be an indication that the stress drop decrease observed in Figure 7,

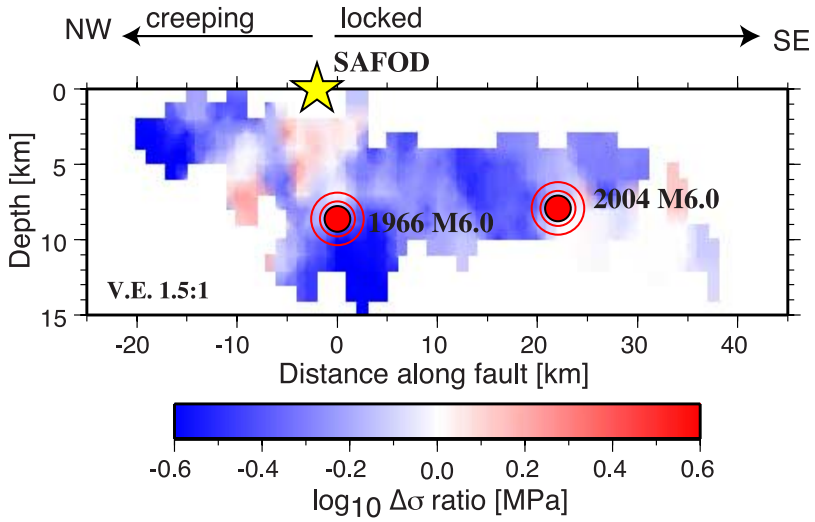

Figure 9. Ratio of stress drop estimates before and after the 2004 M6.0 Parkfield earthquake using a separate processing of the two time periods to correct for possible attenuation changes. Negative values denote a possible increase in stress drop after the event and positive values denote a decrease.

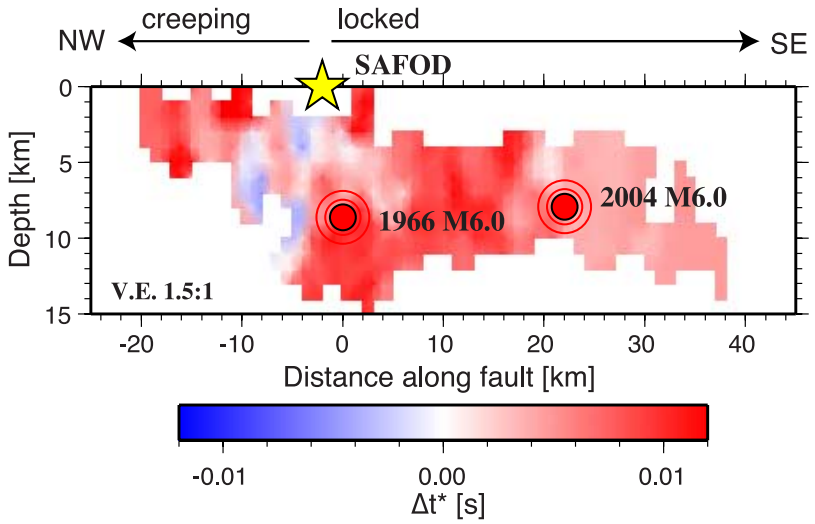

Figure 10. Δt^* variations due to the 2004 M6.0 Parkfield earthquake. Positive areas denote an increase in Δt^* (possible increase in attenuation). The highest increase in Δt^* between the 1966 and 2004 M6.0 events correlates with the slip area of the 2004 event.

although statistically significant, might actually be due to attenuation changes.

[27] We try to resolve this discrepancy by looking at the changes between the separately obtained EGF spectra. For this purpose, we compute the spectral ratio between EGFs before and after the main shock. As before, the spatially varying EGFs are derived for each individual event from the 200 neighboring events, and are thus only valid for the specific location of a particular event. However, the event locations are different before and after the main shock. A means to compare the spatially varying EGFs before and after the main shock is obtained by spatially binning the EGF spectra. This process results in two gridded surfaces for before and after the main shock, where each grid point represents a median EGF spectrum for this location. We divide the EGF spectra for all frequencies at all nonzero grid points in order to obtain the spatially varying spectral ratio over the fault area. The spectral ratio allows us to calculate Δt^*. The parameter t^* is a measure of attenuation along the raypath with $t^* = \int_s Q^{-1}\, dt$. The t^* operator is only a simplification for describing attenuation since Q might be a frequency-dependent quantity. However, the majority of the log spectral ratios form a straight line within our frequency band, and thus provide no indication for frequency-dependent changes in Q in this study.

[28] The value of Δt^* is obtained for each grid point on the fault surface by a linear least squares fit of the spectral ratio between 1 and 50 Hz. We are now using the full frequency range available to us since the EGF spectra are the result of stacking over many neighboring events, thus increasing the signal-to-noise ratio significantly. In principle, these attenuation changes could have occurred anywhere along the raypath but an actual inversion of the obtained Δt^* values for Q is beyond the scope of this paper. However, it seems likely that the strongest changes in material properties would occur in or near the fault zone. Since the Δt^* values stem from source spectra that have already been separated according to equation (1), we can be fairly confident that the obtained Δt^* values are representative of changes inside the fault zone. The variation of Δt^* values for grid points along the fault plane is plotted in Figure 10. Positive Δt^* values indicate an increase in attenuation, whereas negative values point toward a decrease in attenuation along propagation paths from the respective part of the fault surface. We observe the biggest increase in Δt^* in the area between the 1966 and 2004 hypocenters and around the Middle Mountain asperity. The area southeast of the 2004 M6.0 hypocenter shows a less pronounced increase in Δt^*. These results indicate that we may observe significant medium changes due to the main shock. The maximum changes in Δt^* also coincide roughly with the slip area of the 2004 M6.0 event [*Liu et al.*, 2005].

[29] By combining the results for Δt^* variations (Figure 10) and stress drop changes (Figure 7), we can gain an understanding whether the observed spectral changes are due to changes in source parameters or changes in the medium. Any medium changes that we observe (in terms of Δt^*) point toward an increase in attenuation. An increase in attenuation causes a decrease in apparent corner frequency, which would lead to lower stress drop estimates if the attenuation changes were not properly accounted for. We can therefore state that stress drop results may be biased by attenuation increases in areas where we observe a decrease in stress drop, such as around the hypocenter of the 2004 M6.0 event (see Figure 7). In this area, the observed stress drop decrease obtained assuming no changes in propagation path effects may actually be caused by an increase in attenuation, despite its statistical significance. This interpretation is further supported by the fact that the stress drop decrease changes into an increase if we process the data separately before and after the main shock (Figure 9). On the other hand, observed stress drop increases in the Middle Mountain region and along the creeping section cannot be explained by an increase in attenuation. We therefore conclude that the stress drop increase in these areas is actually a real source-related effect rather than caused by structural changes in the fault zone. Indeed it seems likely that the median stress drop increased over most of our

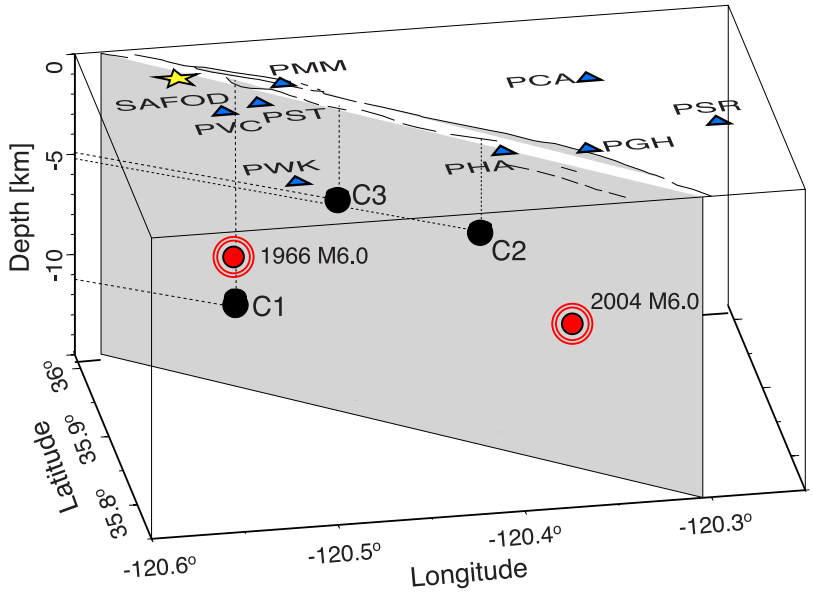

Figure 11. 3-D location map of three repeating earthquake clusters (C1–C3). Seismic stations at the surface are shown as triangles. The gray shaded surface indicates the direction of the San Andreas fault plane. The locations of the 1966 and 2004 hypocenters are shown as big circles.

study area (Figure 9), but the increases near the Middle Mountain asperity and along the creeping section are most reliable because they are seen both with and without the Q correction.

3.6. Repeating Earthquake Clusters

[30] We check the above results by an independent analysis of spectra from repeating cluster microearthquakes. These repeating events, with catalog magnitudes less than 2.5, rupture the same localized fault patches with very regular recurrence intervals. They have identical source parameters and produce nearly identical seismograms at the same stations. Repeating events are therefore often used to identify temporal changes in the medium [see, e.g., *Beroza et al.*, 1995; *Baisch and Bokelmann*, 2001; *Chun et al.*, 2004]. In the Parkfield region these repeating sequences of earthquakes have been found to be quite common [*Nadeau et al.*, 1995; *Nadeau and Johnson*, 1998]. Recently *Sonley and Abercrombie* [2005] have analyzed repeating Parkfield cluster microearthquakes targeting SAFOD and found basically no changes in the medium at shallow depth due to the 2004 main shock. For a deeper cluster they found small changes in the frequency content of the spectra. We partly repeat this analysis here for the purpose of testing our results using an independent data set. We locate 21 multiplets with a cross-correlation coefficient greater or equal than 0.9. Each multiplet consists of at least two event pairs. In the following, we have a closer look at data from three selected clusters that were recorded on the local Northern California Seismic Network (NCSN) stations. The location of the clusters and the stations that recorded them are shown in Figure 11. The clusters sample three regions of the fault in which we observe different stress drop and medium changes.

[31] Figure 12 shows one example event pair for each of the three clusters, recorded on two or three representative local stations. Each pair consists of one event before and one after the 2004 M6.0 main shock. We observe that the waveforms for each pair are nearly identical. When present, differences between events manifest themselves in the high-frequency range of the spectra (middle column), above 20–30 Hz. These differences are quantified by the spectral ratio (Figure 12, right) from which we calculate Δt^*. A horizontal line in the right curve indicates a negligible Δt^* value, and thus no spectral differences between the two events. Keeping this in mind, we observe noticeable spectral changes for cluster C1, located in the Middle Mountain asperity, and cluster C2, located in the region where we observe a stress drop decrease in Figure 7. In contrast, cluster C3 shows no spectral changes due to the main shock, except for station PWK that shows a small change. Station PWK is located due south of the cluster and also a bit farther away. Station PVC and PMM, where no changes are observed for cluster C3 are much closer to the fault, thus raypaths to these stations are more likely to sample significant portions of the fault core. Additional events per cluster (not shown) confirm the observed spectral changes.

[32] Overall, the results from this independent analysis are in accordance to what we observe from Δt^* values computed from the EGF ratios shown in Figure 10: we observe the biggest attenuation changes in the Middle Mountain asperity (cluster C1) and in the area northwest of the 2004 hypocenter (cluster C2). In the area above the 1966 hypocenter (shallower than 7 km, cluster C3), we observe no clear increase in Δt^* in both Figures 10 and 12. In particular, the recordings of cluster C3 at station PMM, which sample exactly this part of the fault zone, do not show a noticeable spectral change. Station PWK is located off to the side, and only a small portion of the raypath

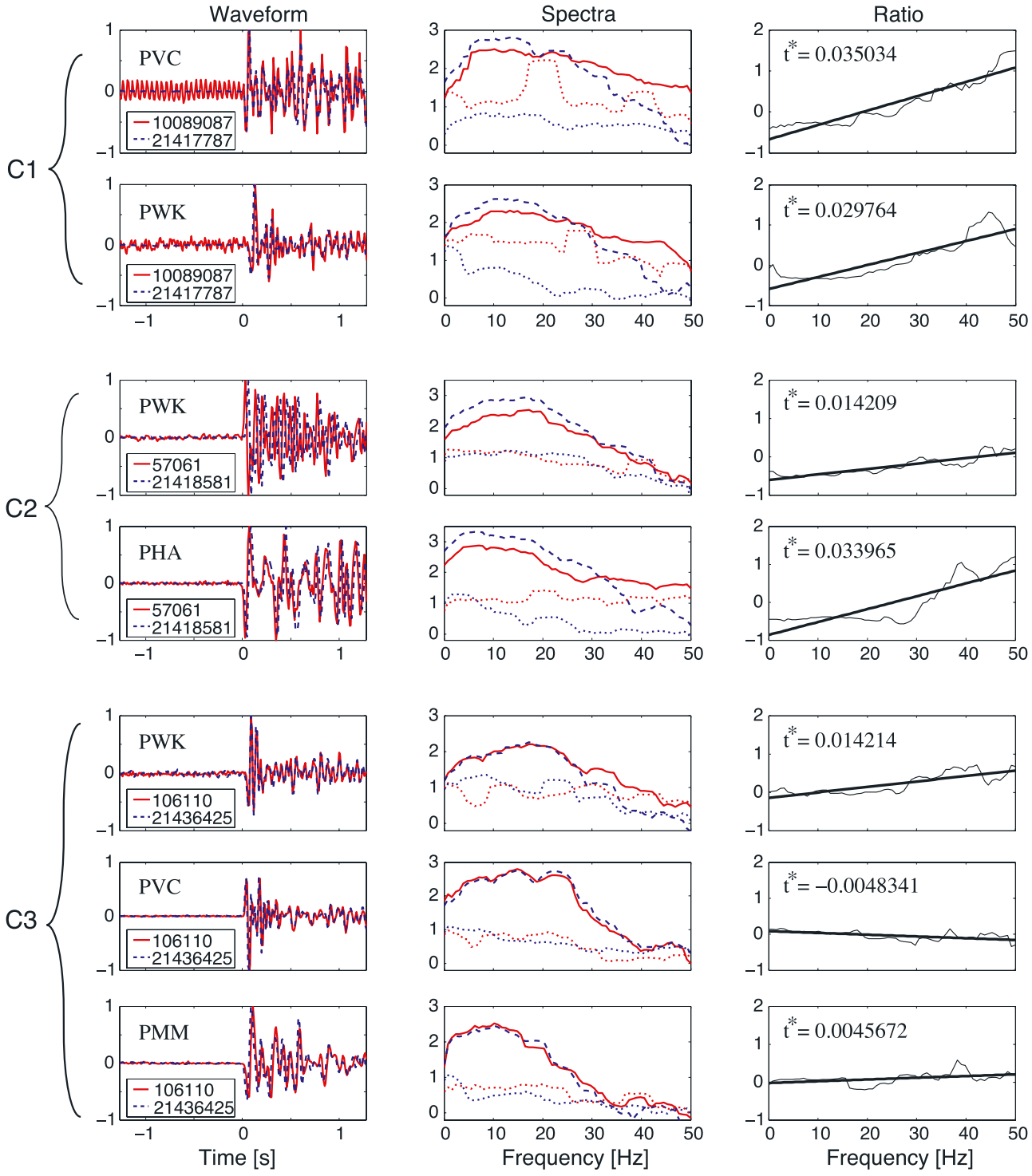

Figure 12. (left) Example waveforms, (middle) spectra, and (right) spectral ratios for three repeating earthquake clusters (C1–C3). The solid line shows the event that occurred before, and the dashed line the event after, the 2004 M6.0 main shock. Dotted lines denote the noise level. Cuspid numbers and station names are shown in the waveform panels. The thick solid lines in the spectral ratio panels show the least squares fit to the data. Δt^* is computed from the slope of the least squares fit.

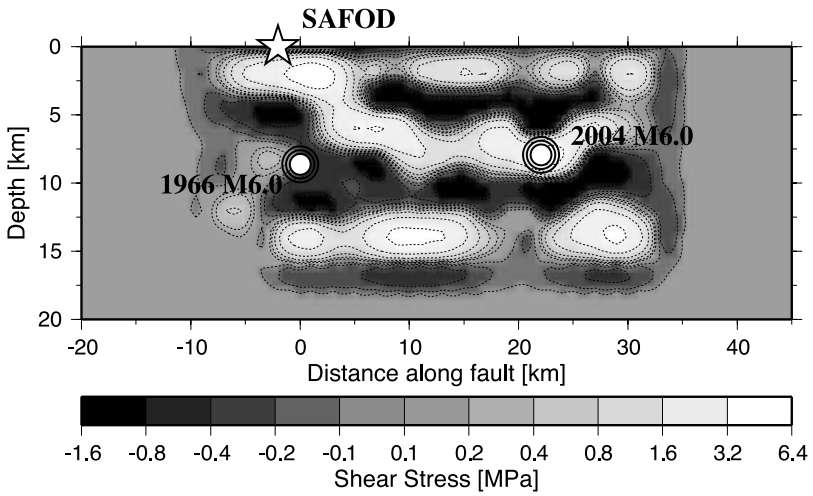

Figure 13. Absolute shear stress changes along the fault plane due to the 2004 M6.0 Parkfield main shock computed from the *Liu et al.* [2005] slip model. Positive values denote a decrease in shear stress, whereas negative values denote an increase in shear stress.

actually travels through the zone affected by the 2004 earthquake. Changes observed at this station could be due to the raypath traveling through a zone of increased attenuation to the southeast of cluster C3.

3.7 Main Shock Shear Stress Changes

[33] Shear stress changes from the main shock are very difficult to constrain since the result depends strongly on the choice and parameterization of the slip model. Nevertheless, we try to estimate these shear stress changes along the fault plane from the slip distribution model of *Liu et al.* [2005] for the 2004 M6.0 Parkfield main shock. Using the method of *Okada* [1992], we compute the strain at depth in an elastic half-space due to a buried finite rectangular source of deformation. We assume a constant shear modulus μ of 3.3×10^4 MPa and unidirectional slip. The SAF is assumed to be a planar, vertically dipping strike-slip fault, extending from the surface to a depth of 20 km. Every rectangular slip patch extends over 1.84 km vertically by 2 km horizontally. The final shear stress changes at every grid point along the fault plane are a summation of all individual slip sources (Figure 13). The resulting shear stress values have been spatially smoothed with a 2 km smoothing length.

[34] As we would expect, we observe a decrease in shear stress in all areas that slipped during the 2004 M6.0 main shock, whereas in surrounding areas the shear stress increases. Remarkably, we observe an increase in main shock-related shear stress change within two depth bands at $\approx$5 km and $\approx$10 km that correlate with seismicity streaks (see Figure 6). The increase of shear stresses around the 1966 M6.0 hypocenter, reaching down to a depth of about 13 km, is between 0.2 and 1.6 MPa, which agrees with our observed statistically significant increase of stress drop estimates in this area (Figure 7). In general, while recognizing the large uncertainties in both measurements, we can state that the stress drop increases that we observe are of the same order of magnitude as the shear stress changes predicted by the slip model. However, we do not observe a significant decrease in stress drops within the slipping regions of the *Liu et al.* [2005] model. Because of the uneven distribution of seismicity, the resolution of our stress drop estimates varies spatially. Whereas we have a high degree of confidence in the median stress drop values obtained for the seismicity streaks, the stress drop estimates are interpolated over the seismicity holes by the nearest neighbor gridding. Therefore, if areas of shear stress decrease in Figure 13 coincide with seismicity holes, they also coincide with areas in which our stress drop estimates (Figure 7) are not as well resolved. We also observe a resolvable increase in median stress drop within the creeping region, which is probably too far from the main shock rupture to have experienced a significant shear stress change. Also, significant postseismic afterslip has been observed from several strainmeters and GPS stations in the Parkfield area [*Langbein et al.*, 2005]. In particular, surface slip detected from field mapping after the main shock was greatest in the Middle Mountain area, i.e., at the northern end of the slip area, and adjacent to the transition to the creeping section. Overall, the response of small earthquake stress drops is likely more complicated than a simple scaling by main shock induced stress changes.

4. Discussion

[35] Our stress drop estimates depend upon our assumed source model and rupture velocity and would increase or decrease if different assumptions were made. However, because we process all of the Parkfield earthquakes in the same way, the relative scales of $\Delta\sigma$ among the events and the locations of the high and low $\Delta\sigma$ regions are robust results. Our observed median stress drop of 6.7 MPa for Parkfield is significantly higher than the median stress drop of 1.6 MPa observed for over 60,000 earthquakes across southern California by *Shearer et al.* [2006]. Because both studies use the same analysis method and assumed source model, it is unlikely that this difference is an artifact. One possible source of bias would be if the northern and southern California local magnitude scales (used in our calibration to moment) had a systematic offset. However, we checked M_L for about 19,000 events common to both

networks and found that their average difference was less than 0.1 and thus too small to explain the observed difference in median stress drop. Compared to most of southern California seismicity, Parkfield has relatively high stress drops, comparable to those seen in the eastern Transverse Ranges by *Shearer et al.* [2006].

[36] The relationship between earthquake stress drops and absolute stress on the fault has been a source of controversy, which relates to the issue of the strength of faults [e.g., *Zoback et al.*, 1987; *Hardebeck and Hauksson*, 1999; *Scholz*, 2000; *Hardebeck and Hauksson*, 2001] and the heat flow paradox [*Lachenbruch and Sass*, 1992]. Our results do not directly address this issue. However, the fact that the patterns of high- and low-stress drop regions on the SAF are largely unchanged by the occurrence of the 2004 M6.0 Parkfield main shock (as shown in Figure 6) suggests either that the main shock released only a small fraction of the background stress on the fault, or that our observed stress drops are controlled more by rock properties than the absolute stress level.

[37] This overall similarity in stress drop patterns before and after the main shock is consistent with studies of other seismic properties in the Parkfield segment that were not affected by the earthquake: *Schorlemmer et al.* [2004] observe a heterogeneous pattern of b values along the Parkfield segment of the SAF, which stayed mostly stationary over the past 35 years. *Waldhauser et al.* [2004] discuss that the seismicity along the fault plane is highly organized in space and time and that larger earthquakes do not seem to change the distribution of seismicity significantly. Figure 6 shows that the aftershocks of the 2004 M6.0 main shock are distributed along the same streaks and form the same seismicity holes as the background seismicity before the main shock.

[38] It should be pointed out that a significant portion (we estimate about 95%) of events after the main shock included in our analysis are part of the aftershock sequence and therefore may have source parameters that differ from the background seismicity. However, our results show a comparable variance of the stress drop results before and after the main shock. Therefore our estimate of temporal stress drop changes assumes aftershocks with no apparent difference in mechanical behavior, compared with the background seismicity. Our data includes events up to June 2005, when the seismicity rate was still about three times above the long-term background rate.

[39] Furthermore, we are not taking into account any short-term temporal changes to the stress drop change imposed by the main shock due to, e.g., healing processes. Fault zone healing has been observed with other seismic methods at several locations in California [e.g., *Li et al.*, 1998, 2003; *Chun et al.*, 2004; *Li et al.*, 2006]. Such changes are difficult to assess with our method since we require a large number of events per grid bin in order to determine spatial variations of source parameters reliably.

[40] Recent studies of *Li et al.* [2004, 2006] have used fault zone trapped waves to image the deep structure of the Parkfield fault zone and found evidence of a $\approx$200 m wide damaged fault core acting as a low-velocity fault zone with significantly lower shear wave velocities than the surrounding rocks. They also observed significant coseismic damage with a shear wave reduction of at least 2.5% caused by the 2004 M6.0 Parkfield earthquake and subsequent postseismic healing processes during the first couple of months after the main shock. These temporal shear wave variations within the fault zone were interpreted to be most likely due to opening and closure of cracks caused by the earthquake. It is possible that a similar mechanism could be causing the attenuation increases that we observe in several areas along the fault. In section 3.2 we showed that our stress drop estimates are very sensitive to shear wave velocity changes (Figure 4). However, *Li et al.* [2006] report that the observed temporal shear wave velocity variations caused by the main shock are strongest only at shallow depth and diminish toward about 5 km depth, indicating that they should not significantly affect our stress drop estimates.

5. Conclusions

[41] From spectral analysis of 4238 earthquakes along the Parkfield segment of the San Andreas fault, we conclude the following:

[42] 1. Small-magnitude earthquakes in this region are self-similar; that is, we observe no dependence of Brune-type stress drop and magnitude.

[43] 2. Our results suggest no depth dependence of estimated stress drops after correcting with a depth-varying shear wave velocity and inferred rupture velocity. However, vertical variations of stress drop estimates are very sensitive to the shear wave velocity model.

[44] 3. After correcting the data with a spatially varying EGF, we observe robust lateral variations of stress drop in the Parkfield segment. The creeping section and the Middle Mountain asperity show significantly lower stress drop values than the rupture area of the 2004 M6.0 earthquake.

[45] 4. We observe statistically significant temporal changes of source spectra before and after the 2004 M6.0 earthquake in some areas of the fault segment.

[46] 5. We are able to distinguish between source effects and near-source attenuation effects. We calculate Δt^* from the spectral ratio of spatially varying EGFs and observe the biggest increase in attenuation in the Middle Mountain asperity and in the region northwest of the 2004 hypocenter. We also observe a significant increase in stress drop estimates in the Middle Mountain asperity and along the creeping section, northwest of SAFOD, which cannot be explained by attenuation changes. The observed temporal stress drop changes are of the same order of magnitude as the main shock shear stress changes computed from existing slip models.

[47] 6. We confirm the observation of temporal changes of attenuation in selected areas of the fault segment by independently analyzing repeating earthquake clusters.

Appendix A

[48] Here we describe a simple synthetic test to better explain the performance of our approach and to confirm the ability of our method to isolate the source term from the observed spectra, even if the corner frequency exceeds the upper end of the fitting range (20 Hz). We calculate synthetic source spectra for the actual event distribution at

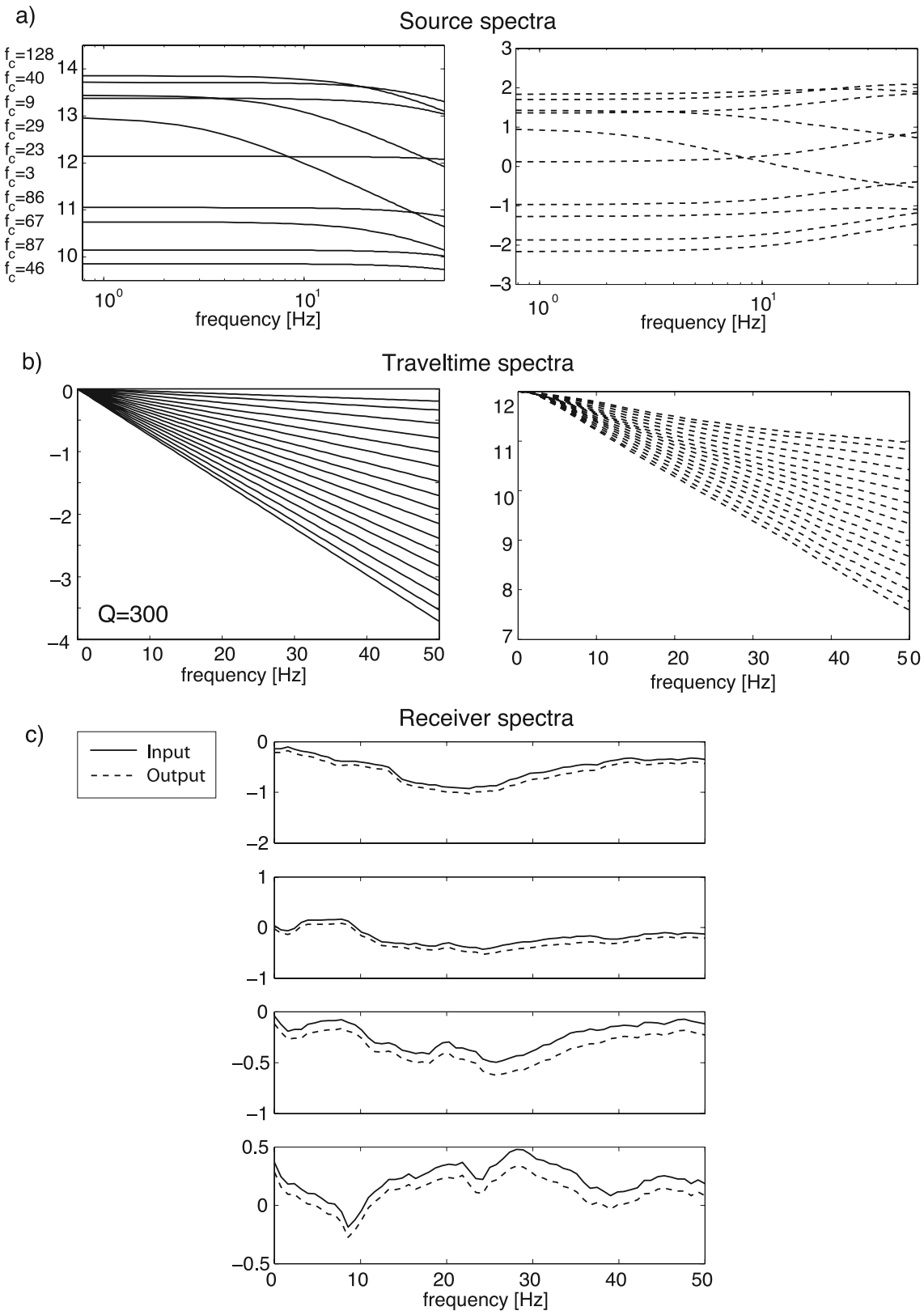

Figure A1. Synthetic (solid) and inverted (dashed) spectral terms for (a) source term for 10 example events. The difference between input and output source spectra corresponds to the EGF correction spectrum, determined in a subsequent step. (b) Traveltime term for 30 traveltime bins of 1 s each. (c) Input and output receiver terms at four selected stations.

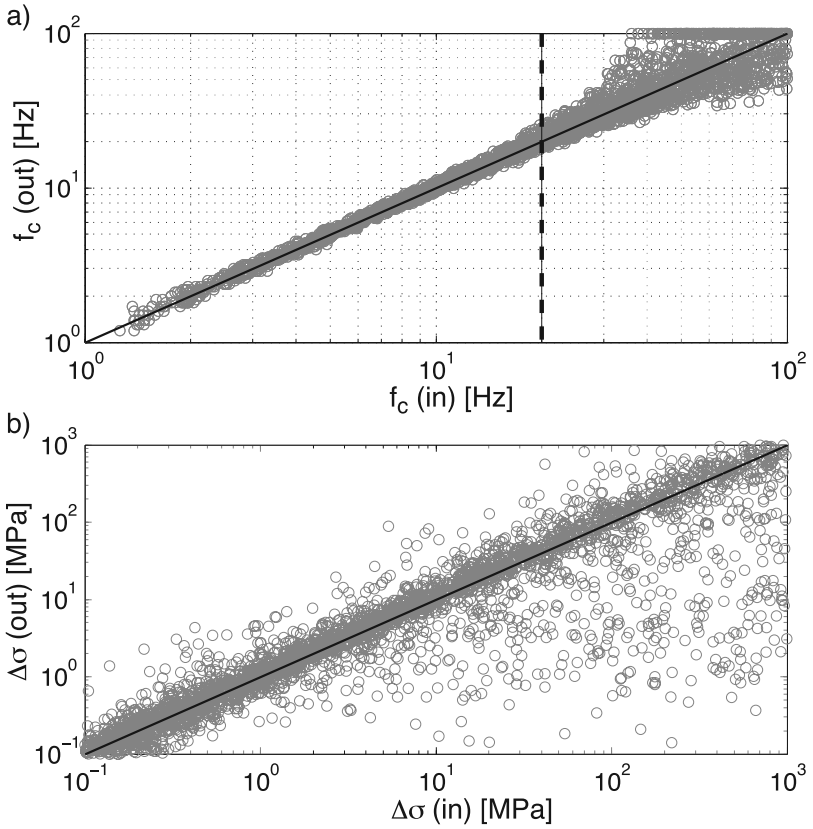

Figure A2. Synthetic input versus inverted output for (a) corner frequency and (b) stress drop. The vertical dashed line in the top panel marks the upper fitting boundary of f_c = 20 Hz.

Parkfield following equations (2) and (5) by randomly selecting magnitudes (0.5–3.5) and stress drops (0.1–1000 MPa) and assuming a constant shear wave velocity (β = 3.5 km/s). Following equation (1), we add synthetic traveltime terms, calculated for a constant Q of 300, and the actual receiver spectral terms obtained from the real data. These synthetic displacement spectra are then put into the inversion algorithm. Comparisons between the original spectra and the estimated spectra for the source, traveltime, and receiver terms are shown in Figure A1 for 10 example events. Note that as expected the absolute shapes of the source spectra are not resolved but that their relative shapes are accurately recovered. We then apply the same processing parameters used for analysis of the real data to compute corner frequencies f_c and stress drops $\Delta\sigma$. Figure A2 shows a comparison of input and output f_c (top) and $\Delta\sigma$ (bottom). Note that the accuracy of the f_c determination gradually deteriorates beyond the fitting range of 20 Hz (dashed line). Despite the increased scatter, the points in the f_c cross plot are still centered around the line given by f_c (in) = f_c (out) (solid line). We are able to estimate corner frequencies above the fitting range of 20 Hz, albeit with increasing uncertainties as the corner frequency exceeds the fitting range. It should be noted that the above result does not change significantly for a fitting range up to 40 Hz. However, for real Parkfield data, the S/N ratio generally deteriorates with increasing frequency. This leads to a trade-off between uncertainties introduced by a lower S/N ratio and uncertainties introduced by lowering the fitting range. The choice of 20 Hz as upper boundary of the fitting range is a compromise reflecting this trade-off.

[49] **Acknowledgments.** We thank Guoqing Lin for help in extracting the waveform data and relocating our events and Germán Prieto for providing his multitaper code. We are grateful to C. Thurber for providing a copy of his 3-D velocity model of the SAFOD area. We wish to thank Alexander Goertz for fruitful discussions and Takuj Yamada and an anonymous reviewer for comments that helped to improve the manuscript. This research was funded by NEHRP/USGS grant 03HQPA0001 and supported by the Southern California Earthquake Center. SCEC is funded by NSF Cooperative Agreement EAR-0106924 and USGS Cooperative Agreement 02HQAG0008. SCEC contribution 978.

References

Abercrombie, R. (1995), Earthquake source scaling relationships from −1 to 5 ML using seismograms recorded at 2.5 km depth, *J. Geophys. Res.*, *100*, 24,015–24,036.

Abercrombie, R. (2000), Crustal attenuation and site effects at Parkfield, California, *J. Geophys. Res.*, *105*, 6277–6286.

Aki, K. (1967), Scaling law of seismic spectrum, *J. Geophys. Res.*, *72*, 1217–1231.

Anderson, J. (1986), Implication of attenuation for studies of the earthquake source, in *Earthquake Source Mechanics*, *Geophys. Monogr. Ser.*, vol. 37, edited by S. Das, J. Boatwright, and C. H. Scholz, pp. 311–318, AGU, Washington, D. C.

Andrews, D. (1986), Objective determination of source parameters and similarity of earthquakes of different size, in *Earthquake Source Mechanics*, *Geophys. Monogr. Ser.*, vol. 37, edited by S. Das, J. Boatwright, and C. H. Scholz, pp. 259–267, AGU, Washington, D. C.

Archuleta, R., E. Cranswick, C. Mueller, and P. Spudich (1982), Source parameters of the 1980 Mammoth Lakes, California, earthquake sequence, *J. Geophys. Res.*, *87*, 4595–4607.

Baisch, S., and G. Bokelmann (2001), Seismic waveform attributes before and after the Loma Prieta earthquake: Scattering change near the earthquake and temporal recovery, *J. Geophys. Res.*, *106*, 16,323–16,337.

Beroza, G., A. Cole, and W. Ellsworth (1995), Stability of coda wave attenuation during the Loma Prieta, California, earthquake sequence, *J. Geophys. Res.*, *100*, 3977–3987.

Boatwright, J. (1984), Seismic estimates of stress release, *J. Geophys. Res.*, *89*, 6961–6968.

Brune, J. (1970), Tectonic stress and spectra of seismic shear waves from earthquakes, *J. Geophys. Res.*, *75*, 4997–5009.

Brune, J., R. Archuleta, and S. Hartzell (1979), Far-field S wave spectra, corner frequencies, and pulse shapes, *J. Geophys. Res.*, *84*, 2262–2272.

Chavarria, J., P. Malin, and E. Shalev (2004), The SAFOD Pilot Hole seismic array: Wave propagation effects as a function of sensor depth and source location, *Geophys. Res. Lett.*, *31*, L12S07, doi:10.1029/2003GL019382.

Chun, K.-Y., G. A. Henderson, and J. Liu (2004), Temporal changes in P wave attenuation in the Loma Prieta rupture zone, *J. Geophys. Res.*, *109*, B02317, doi:10.1029/2003JB002498.

Eberhart-Phillips, D., and A. Michael (1993), Three-dimensional velocity structure, seismicity, and fault structure in the Parkfield region, central California, *J. Geophys. Res.*, *98*, 15,737–15,758.

Eshelby, J. (1957), The determination of the elastic field of an ellipsoidal inclusion, and related problems, *Proc. R. Soc. London, Ser. A*, *241*, 376–396.

Fletcher, J., and M. Guatteri (1999), Stress Drop for three M 4.3–4.7 (1992–1994) Parkfield, CA, earthquakes, *Geophys. Res. Lett.*, *26*, 2295–2298.

Fletcher, J., and P. Spudich (1998), Rupture characteristics of the three M 4.7 (1992–1994) Parkfield earthquakes, *J. Geophys. Res.*, *103*, 835–854.

Hardebeck, J., and E. Hauksson (1997), Static stress drop in the 1994 Northridge, California, aftershock sequence, *Bull. Seismol. Soc. Am.*, *87*, 1495–1501.

Hardebeck, J., and E. Hauksson (1999), Role of fluids in faulting inferred from stress field signatures, *Science*, *285*, 236–239.

Hardebeck, J., and E. Hauksson (2001), Crustal stress field in southern California and its implications for fault mechanics, *J. Geophys. Res.*, *106*, 21,859–21,882.

Hough, S. (1996), Observational constraints on earthquake source scaling: Understanding the limits in resolution, *Tectonophysics*, *261*, 83–95.

Hough, S. (1997), Empirical Green's function analysis: Taking the next step, *J. Geophys. Res.*, *102*, 5369–5380.

Ide, S., and G. Beroza (2001), Does apparent stress vary with earthquake size?, *Geophys. Res. Lett.*, *28*, 3349–3352.

Ide, S., G. C. Beroza, S. G. Prejean, and W. L. Ellsworth (2003), Apparent break in earthquake scaling due to path and site effects on deep borehole recordings, *J. Geophys. Res.*, *108*(B5), 2271, doi:10.1029/2001JB001617.

Imanishi, K., W. Ellsworth, and S. G. Prejean (2004), Earthquake source parameters determined by the SAFOD Pilot Hole seismic array, *Geophys. Res. Lett.*, *31*, L12S09, doi:10.1029/2004GL019420.

Jones, L., and D. Helmberger (1996), Seismicity and stress-drop in the eastern Transverse ranges, southern California, *Geophys. Res. Lett.*, *23*, 233–236.

Kanamori, H., and D. Anderson (1975), Theoretical basis of some empirical relations in seismology, *Bull. Seismol. Soc. Am.*, *65*, 1023–1095.

Korneev, V., R. Nadeau, and T. McEvilly (2003), Seismological studies at Parkfield IX: Fault-zone imaging using guided wave attenuation, *Bull. Seismol. Soc. Am.*, *93*, 1415–1426.

Lachenbruch, A., and J. Sass (1992), Heat flow and energetic of the San Andreas Fault Zone, *J. Geophys. Res.*, *85*, 6185–6223.

Langbein, J., et al. (2005), Preliminary report on the 28 September 2004 M 6.0 Parkfield, California earthquake, *Seismol. Res. Lett.*, *76*(1), 10–26.

Li, Y.-G., J. Vidale, K. Aki, F. Xu, and T. Burdette (1998), Evidence of shallow fault zone strengthening after the 1992 M7.5 Landers, California, earthquake, *Science*, *279*, 217–219.

Li, Y.-G., J. Vidale, S. Day, D. Oglesby, and E. Cochran (2003), Postseismic fault healing on the rupture zone of the 1999 M7.1 Hector Mine, California, earthquake, *Bull. Seismol. Soc. Am.*, *93*, 854–869.

Li, Y.-G., J. Vidale, and E. Cochran (2004), Low-velocity damaged structure of the San Andreas Fault at Parkfield from fault zone trapped waves, *Geophys. Res. Lett.*, *31*, L12S06, doi:10.1029/2003GL019044.

Li, Y-.G., P. Chen, E. Cochran, J. Vidale, and T. Burdette (2006), Seismic evidence for rock damage and healing on the San Andreas Fault associated with the 2004 M6 Parkfield earthquake, *Bull. Seismol. Soc. Am.*, *96*, 349–363.

Lin, G., and P. Shearer (2005), Tests of relative earthquake location techniques using synthetic data, *J. Geophys. Res.*, *110*, B04304, doi:10.1029/2004JB003380.

Liu, P., S. Custódio, and R. Archuleta (2005), Kinematic inversion of the 2004 M_w 6.0 Parkfield earthquake including an approximation to site effects, *Bull. Seismol. Soc. Am.*, *96*, 143–158.

Madariaga, R. (1976), Dynamics of an expanding circular fault, *Bull. Seismol. Soc. Am.*, *66*, 639–666.

Michelini, A., and T. McEvilly (1991), Seismological studies at Parkfield I: Simultaneous inversion for velocity structure and hypocenters using cubic B-splines parameterization, *Bull. Seismol. Soc. Am.*, *81*, 524–552.

Mueller, C. (1985), Source pulse enhancement by deconvolution of an empirical Green's function, *Geophys. Res. Lett.*, *12*, 33–36.

Murray, J., and S. Segall (2005), Spatiotemporal evolution of a transient slip event on the San Andreas fault near Parkfield, California, *J. Geophys. Res.*, *110*, B09407, doi:10.1029/2005JB003651.

Nadeau, R., and L. Johnson (1998), Seismological studies at Parkfield VI: Moment release rates and estimates of source parameters for small repeating earthquakes, *Bull. Seismol. Soc. Am.*, *88*, 790–814.

Nadeau, R., W. Foxall, and T. McEvilly (1995), Clustering and periodic recurrence of microearthquakes on the San Andreas Fault at Parkfield, California, *Science*, *267*, 503–507.

Okada, Y. (1992), Internal deformation due to shear and tensile faults in a half-space, *Bull. Seismol. Soc. Am.*, *82*, 1018–1040.

Park, J., C. Lindberg, and F. Vernon (1987), Multitaper spectral analysis of high-frequency seismograms, *J. Geophys. Res.*, *92*, 12,675–12,648.

Prejean, S., and W. Ellsworth (2001), Observations of earthquake source parameters at 2 km depth in the Long Valley Caldera, eastern California, *Bull. Seismol. Soc. Am.*, *91*, 165–177.

Prieto, G., P. M. Shearer, F. L. Vernon, and D. Kilb (2004), Earthquake source scaling and self-similarity estimation from stacking P and S spectra, *J. Geophys. Res.*, *109*, B08310, doi:10.1029/2004JB003084.

Roeloffs, E., and J. Langbein (1994), The earthquake prediction experiment at Parkfield, California, *Rev. Geophys.*, *32*, 315–336.

Scholz, C. (2000), Evidence for a strong San Andreas fault, *Geology*, *28*(2), 163–166.

Schorlemmer, D., S. Wiemer, and M. Wyss (2004), Earthquake statistics at Parkfield: 1. Stationarity of b values, *J. Geophys. Res.*, *109*, B12307, doi:10.1029/2004JB003234.

Shearer, P., E. Hauksson, and G. Lin (2005), Southern California hypocenter relocation with waveform cross-correlation, part 2: Results using source-specific station terms and cluster analysis, *Bull. Seismol. Soc. Am.*, *95*(3), 904–915, doi:10.1785/0120040168.

Shearer, P., G. Prieto, and E. Hauksson (2006), Comprehensive analysis of earthquake source spectra in southern California, *J. Geophys. Res.*, *111*, B06303, doi:10.1029/2005JB003979.

Smith, W., and P. Wessel (1990), Gridding with continuous curvature splines in tension, *Geophysics*, *55*, 293–305.

Snoke, J. (1987), Stable determination of (Brune) stress drops, *Bull. Seismol. Soc. Am.*, *77*, 530–538.

Sonley, E., and R. Abercrombie (2005), The effect of the 2004 M6.0 earthquake on small repeating earthquakes recorded downhole at Parkfield, *Eos Trans. AGU*, *86*(52), Fall Meet. Suppl., Abstract S33C-05.

Thurber, C., S. Roecker, K. Roberts, M. Gold, L. Powell, and K. Rittger (2003), Earthquake locations and three-dimensional fault zone structure along the creeping section of the San Andreas fault near Parkfield, CA: Preparing for SAFOD, *Geophys. Res. Lett.*, *30*(3), 1112, doi:10.1029/2002GL016004.

Thurber, C., S. Roecker, H. Zhang, S. Baher, and W. Ellsworth (2004), Fine-scale structure of the San Andreas fault zone and location of the SAFOD target earthquakes, *Geophys. Res. Lett.*, *31*, L12S02, doi:10.1029/2003GL019398.

Venkataraman, A., and H. Kanamori (2004a), Observational constraints on the fracture energy of subduction zone earthquakes, *J. Geophys. Res.*, *109*, B05302, doi:10.1029/2003JB002549.

Venkataraman, A., and H. Kanamori (2004b), Effect of directivity on estimates of radiated seismic energy, *J. Geophys. Res.*, *109*, B04301, doi:10.1029/2003JB002548.

Waldhauser, F., W. L. Ellsworth, D. P. Schaff, and A. Cole (2004), Streaks, multiplets, and holes: High-resolution spatio-temporal behavior of Parkfield seismicity, *Geophys. Res. Lett.*, *31*, L18608, doi:10.1029/2004GL020649.

Wallace, R. E. (1990), The San Andreas fault system, California, *U.S. Geol. Surv. Prof. Pap.*, 1515.

Warren, L. M., and P. M. Shearer (2002), Mapping lateral variations in upper mantle attenuation by stacking *P* and *PP* spectra, *J. Geophys. Res.*, *107*(B12), 2342, doi:10.1029/2001JB001195.

Zoback, M., et al. (1987), New evidence of the state of stress of the San Andreas Fault System, *Science*, *238*, 1105–1111.

B. Allmann and P. Shearer, IGPP-0225, SIO, University of California, San Diego, 9500 Gilman Drive, La Jolla, CA 92093-0225, USA. (ballmann@ucsd.edu; pshearer@ucsd.edu)